Failure and size effect for notched and unnotched concrete beams[‡]

D. Grégoire, L. B. Rojas-Solano and G. Pijaudier-Cabot[*,†]

Laboratoire des Fluides Complexes et leurs Réservoirs, LFC-R UMR5150, Université de Pau et des Pays de l'Adour, Allée du Parc Montaury, F64600 Anglet, France

SUMMARY

Modelling failure in geomaterials, concrete or other quasi-brittle materials and proper accounting for size effect, geometry and boundary effects are still pending issues. Regularised failure models are capable of describing size effect on specimens with a specific geometry, but extrapolations to other geometries are rare, mostly because experimental data presenting size effect for different geometries and for the same material are lacking. Three-point bending fracture tests of geometrically similar notched and unnotched specimens are presented. The experimental results are compared with numerical simulations performed with an integral-type non-local model. Comparisons illustrate the shortcomings of this classical formulation, which fails to describe size effect over the investigated range of geometries and sizes. Finally, experimental results are also compared with the universal size effect law. Copyright © 2013 John Wiley & Sons, Ltd.

1. INTRODUCTION

Modelling failure in geomaterials, concrete or other quasi-brittle materials includes a proper description of size, geometry and boundary effects. Quasi-brittle materials exhibit a fracture process zone (FPZ) surrounding the crack tip whose size is not negligible compared with the structure size (in concrete, the FPZ size is equal to 3–6 times the maximum aggregate size approximately, i.e. tenth of centimetres). This is the main reason why linear elastic fracture mechanics does not apply. In the classical examples of geometrically similar structures, the ratio of the size of the FPZ to the size of the structure is not constant and a decrease of the nominal stress with an increase of the structure size is observed. This is commonly called 'structural size effect'. It is deterministic, and it depends on the geometry of the specimen. Moreover, the FPZ shape and the FPZ size are different if the fracture initiates from a flat boundary (unnotched specimen) or from a notch. On top, the FPZ expansion may be constrained close to a boundary. These two phenomena are usually merged and denoted as 'boundary effects'. Size and boundary effects might be important engineering issues because (i) the design of the large structures relies on material properties measured at the laboratory scale, and (ii) in most instances, cracks initiate from the surface of the structure where boundary effect exists.

Size effects have been investigated by scientists for years in different contexts and for different materials. The pioneers have been Leonardo da Vinci (1452–1519), Galileo Galilei (1564–1642) (tension tests on marble columns), Edme Mariotte (1620–1684) (tension tests on iron wire) and Georges-Louis Leclerc de Buffon (1707–1788) (three-point bending tests on wood). Intensive studies of size effect in quasi-brittle materials started from the middle of the 20th century (e.g. [1–4]). Experiments involving

---

*Correspondence to: G. Pijaudier-Cabot, Laboratoire des Fluides Complexes et leurs Réservoirs, LFC-R UMR5150, Université de Pau et des Pays de l'Adour, Allée du Parc Montaury, F64600 Anglet, France.

†E-mail: gilles.pijaudier-cabot@univ-pau.fr
‡Supporting information may be found in the online version of this article

size effect have been carried out on many materials, such as concrete (e.g. [5, 6]), mortar (e.g. [7]), marble (e.g. [8]), sandstone (e.g. [9]), brittle ceramic (e.g. [10]), wood (e.g. [11]) or polymers (e.g. [12]), under pure tension, bending or shear. At the same time, different theories for describing size effect have been promoted in the literature such as the energetic-statistical theory (e.g. [11, 13, 14]), the fractal theory (e.g. [15]) or the Weibull-statistical theory (e.g. [9]). The present study aims at stetting the scene for future elements of validation of constitutive models. More precisely, an assessment of their capability of describing size effect from non-linear finite element computations is targeted. To this end, documented size effect test data are required for various geometries, on the same material.

Classical failure constitutive models involve strain softening due to progressive cracking and a regularisation technique for avoiding spurious strain and damage localisation. Different approaches have been promoted in the literature such as integral-type non-local models (e.g. [16]), gradient damage formulations (e.g. [17]), cohesive cracks models (e.g. [18] with classical finite elements and e.g. [19] with extended finite elements) or strong discontinuity approaches (e.g. [20]). Such macroscale failure models have been applied on a wide range of problems, including the description of damage and failure in strain softening quasi-brittle materials [16], softening plasticity [21–23], creep [24] or composite degradation [25]. They may exhibit, however, some inconsistencies such as (i) incorrect crack initiation, ahead of the crack tip; (ii) propagating damage fronts after failure due to non-local averaging; (iii) incorrect shielding effect with non-zero non-local interactions across a crack surface; and (iv) deficiencies at capturing spalling properly in dynamics, with spalls of zero thickness when the expected spall size is below the internal length of the model (e.g. [26–29]).

Aside these problems, which have been addressed in the aforementioned references, an important element of validation of failure models is that they should be able to capture size and boundary effects for various geometries. On a specific geometry, typically on three-point bending tests on geometrically similar notched beams with a fixed notch-to-beam depth ratio, size effect test data can be used for the calibration of model parameters (e.g. [30, 31]). In [27], however, it was shown from numerical examples that the classical non-local isotropic damage model cannot capture structural size effect for notched and unotched specimens at the same time, with the same set of test data. In other words, the model is not capable of describing structural size effect properly unless it has been calibrated on the same specific geometry. Numerical predictions of size effect on different geometries or the description of boundary effects are however quite rare in the literature because experimental data on different specimen geometries and on the same material are not available for comparison. If experiments involving size effect are numerous in the literature, they are restricted to a specific geometry and barely consider structures made of the same material, with different geometries. Most of the time, the notch-to-depth ratio tends to zero without reaching zero (e.g. [32, 33]), and unnotched specimens are studied separately (e.g. [34]), with different materials compared with size effect tests on notched specimens. Recent studies involved both notched and unnotched specimens (e.g. [6, 35]). They are not complete in the sense that all notch configurations are not studied in regard of all beam depth configurations.

Providing such experiments is the major objective of the present study. Section 2 is dedicated to the description of experiments performed on geometrically similar notched and unnotched concrete specimens made of the same mix. Three different geometries have been considered to obtain results involving size and boundary effects at the same time. In Section 3, the shortcomings of the classical integral-type non-local damage model, with respect to the description of size and boundary effect, are briefly outlined.

Finally, a fit of the experimental data with a general size effect formula is provided. If the size effect formulae provide trends that are consistent with experiments, a correct agreement between numerical finite element calculations and these formulae is an element of positive appreciation of the consistency of failure models. It is with this objective in mind that comparisons between experimental data and size effect laws is discussed and our intent is not to claim that one size effect law is better than another. It should be kept in mind that size effect formulae provide a fit of the evolution of the maximum stress with the structure size only. The present experiments provide the entire load deflection curves, and it is much more demanding for failure models to be able to capture the entire structural response for various geometries and various sizes at the same time than to capture peak loads only. The present experimental data provide the ground for such future comparisons.

Table I. Concrete mixture formulation.

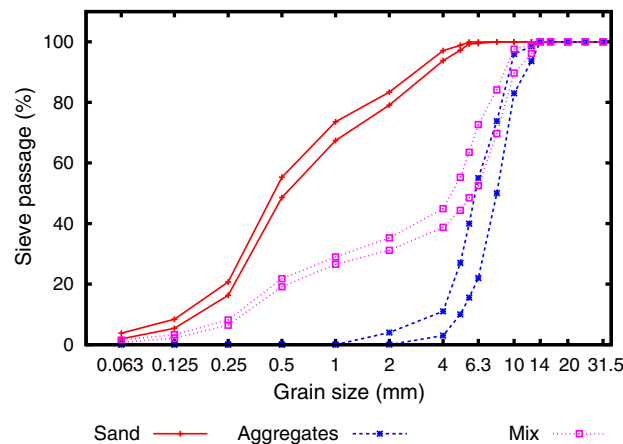| Product	Designation	Mass (kg)
Sand	Cemex 0/4	740
Aggregates	Durruty 4/10	1140
Cement	Calcia CEM II/A	286
Admixture	Axim Cimplast 115	1
Water	Clarified water	179
	Total	2346

Figure 1. Sand, aggregates and mix gradings.

2. EXPERIMENTAL STUDY

2.1. Material, specimens and test rig descriptions

The concrete formulation is based on a ready-mix concrete mixture obtained from Unibéton for paving slab applications. The formulation is detailed in Table I, and the gradings of the sand, the coarse aggregate and the mix are presented in Figure 1.

The experiments deal mainly with bending beams of different sizes. All tested beams were made with the same mix shown in Table I. However, eight batches were needed to manufacture the specimens with a 150-L concrete mixer. Specimens were removed from their moulds 24 h after casting and then stored in water at room temperature. They were removed from water 24 h before testing. The mechanical test did not last more than 1 h for each specimen. Note that no particular attention was paid at possible drying effects. The same experimental routine has been performed so that the possible bias introduced by drying is the same for all the specimens approximately.

To characterise the material properties of each batch of concrete and to check the global reproducibility, standard compressive tests and splitting (Brazilian) tests were performed following European standards (EN 12390-1-3-6[§]). A total of 51 standard cylinders (with a height-to-diameter ratio of 2) were manufactured, from the material taken out from the eight batches, in addition to the beams. Compressive strength,[¶] splitting tensile strength, Young's modulus[‖] and Poisson ratio[**] were thus measured, and Table II presents the results in terms of mean values, standard deviations and coefficients of variation. In addition, Appendix A provides the different material properties for each batch

---

[§]Testing hardened concrete – Part 1, Part 3 and Part 6.
[¶]Cylinders are rectified to ensure smooth and parallel surfaces (no capping compound).
[‖]Local strain is measured through three Epsilon tech sensors (#3542-050M-050-ST) to avoid bending effects.
[**]Lateral expansion is measured through Epsilon tech sensor (#3442-010M-005-ST).

Table II. Concrete mean mechanical properties.

Compressive strength			Young modulus			Poisson ratio			Splitting tensile strength		
μ (MPa)	σ (MPa)	c_v (%)	μ (GPa)	σ (GPa)	c_v (%)	μ (–)	σ (–)	c_v (%)	μ (MPa)	σ (MPa)	c_v (%)
42.3	2.8	6.6	37.0	0.9	2.4	0.21	0.02	8.7	3.9	0.2	6.0

μ, mean value; σ, standard deviation; $c_v = \mu/\sigma$, coefficient of variation.
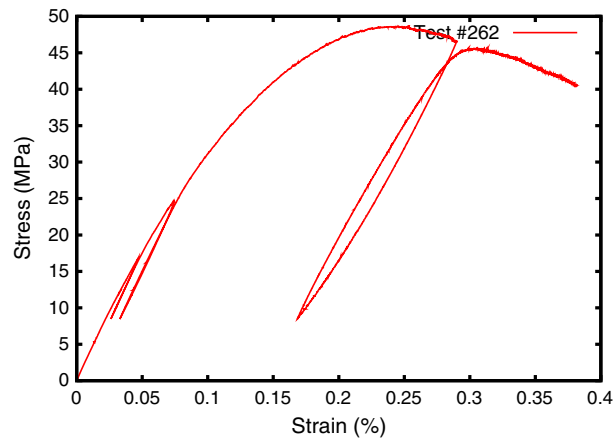

Figure 2. Stress–strain curve in uniaxial compression obtained for test #262 of batch #2.

(Tables A.1–A.4). Figure 2 presents the stress–strain curve obtained for cylinder #262 of batch #2 in uniaxial compression. Material characterisation and structural testing were performed at the same age for each batch plus or minus 2 days, and no ageing influence was observed as presented in Figure 3 except some classical dispersion.

In the bending tests, four different sizes of geometrically similar specimens were considered, with a span-to-depth ratio of 2.5, a depth varying between 50 and 400 mm and a constant thickness of 50 mm. To exhibit some boundary effect, three different (moulded) notch configurations were used. Note that the notch thickness was kept constant (2 mm) whatever the specimen depth. They are labelled: *unnotched* (notch-to-depth ratio of 0), *fifth-notched* (notch-to-depth ratio of 0.2) and *half-notched* (notch-to-depth ratio of 0.5). For each size and each notch configuration, three concrete beams were manufactured. Overall, 34 three-point bending tests have been carried out. The different beam specimen geometries are presented in Figure 4.

The testing apparatus is a three-point bend setup mounted on a servo-hydraulic testing machine (HB250, Zwick/Roell, Metz, France). To avoid post-peak unstable crack propagation, the three-point bending tests are crack mouth opening displacement (CMOD) controlled. The CMOD measurement consists in recording the distance between two alumina plates glued on the bottom surface of the beam, on each side of the initial notch. When the beam is unnotched, the alumina plates are glued at a distance from mid-span equal to half the depth of the beam to ensure that the crack initiates between the two plates (Figure 5). In this case, the relative distance between the aluminina plates is not a CMOD. Still, in the case of unnotched structures, this relative displacement will be denoted as a CMOD for the sake of simplicity of the presentation. The resulting force is measured by a 50-kN load cell, in addition to the 250-kN load cell available with the machine. The deflection of the neutral axis is measured using a laser sensor with a setup that eliminates the deformation at the supports (similar to that e.g. in Ref. [7]). All signals were recorded and synchronised through a multichannel digital controller. Figure 6 presents the different raw data measured by each sensor during a test corresponding to $(i, n) = (2, 2)$ (Figure 4), and Table III summarises the uncertainties of the different sensors provided by the manufacturer.
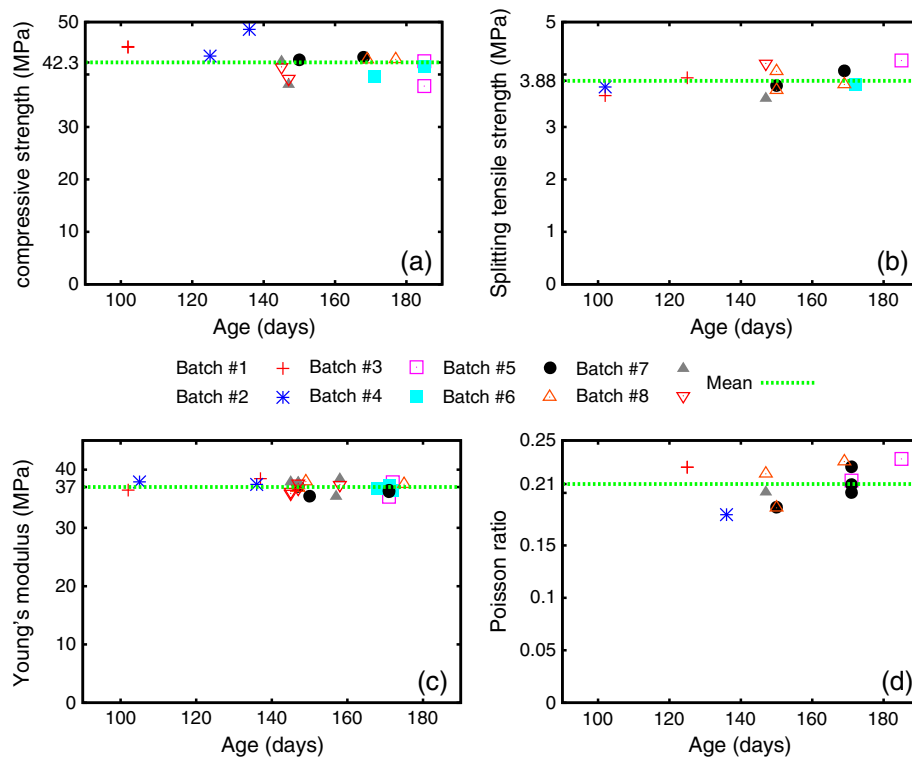
Figure 3. Ageing influence on mechanical properties: (a) compressive strength; (b) splitting tensile strength; (c) Young's modulus; (d) Poisson ratio.
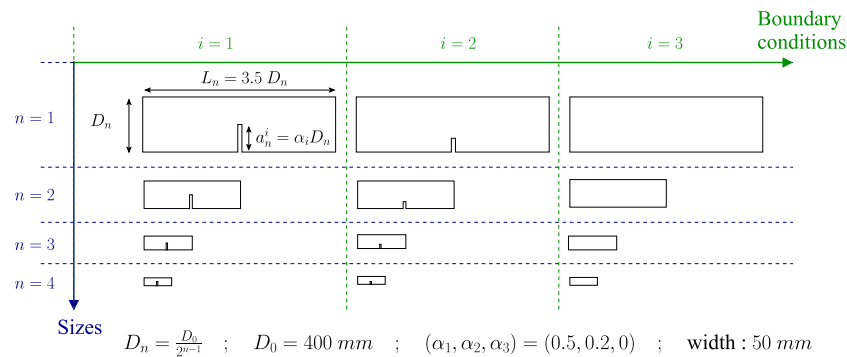

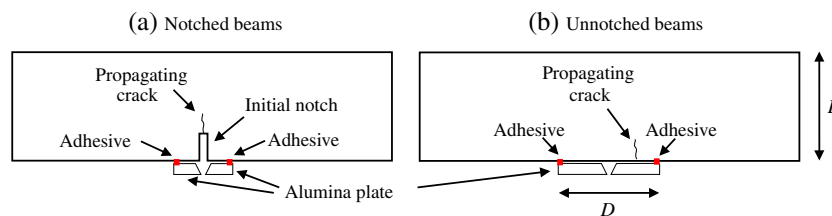Figure 4. Beam specimen geometries.

Figure 5. Crack mouth opening displacement measurement for (a) notched and (b) unnotched beams.
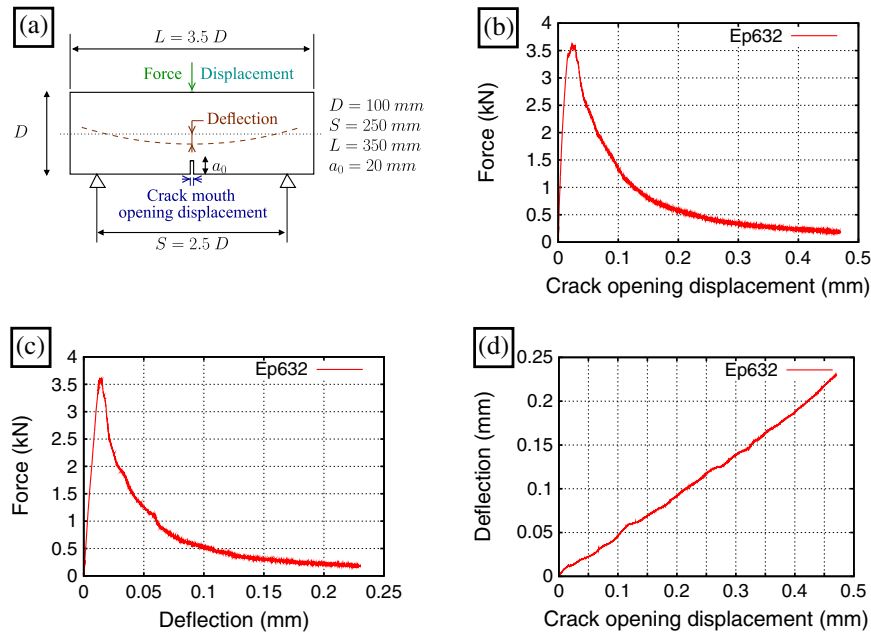
Figure 6. Raw data measured by each sensor during a test: (a) geometry and measurements; (b) force versus crack mouth opening displacement (CMOD) raw data; (c) force versus deflection raw data; (d) deflection versus CMOD raw data.

Table III. Uncertainties of the different sensors provided by the manufacturer.

Relative uncertainties		Absolute uncertainties	
Measurements	Uncertainty	Measurements	Uncertainty
CMOD	±0.25%	Displacement	±0.5 mm
Force (250 kN)	±0.25%	Force (50 kN)	±25 N
Force (50 kN)	±0.25%	Deflection	±0.5 μm

2.2. Experimental results on the bending beams

The experiments have been performed following the RILEM[††] recommendations [36]. The results of 13 half-notched specimens, 11 fifth-notched and 10 unnotched specimens are reported in this study (notch-to-depth ratio of 0.5, 0.2 and 0, respectively; span-to-depth ratio of 2.5; depth varying between 50 and 400 mm). The actual beam geometries and peak loads are collected in Tables B.1–B.3 in Appendix B. Figure 7 shows the average load versus CMOD responses for the four sizes and the three geometries. Appendix B shows also the Force versus CMOD data of each specimen (Figures B.1–B.3).

At first, let us collect and compare the ligament strength for each size and each geometry. The ligament strength is defined as the maximum stress in the ligament at peak load. It is denoted as σ_{lig} (Equation (1)).

$$\sigma_{\text{lig}} = \frac{3}{2} \frac{FS}{bh^2} \tag{1}$$

where F is the load and S, b and h are the span, the width and the ligament height, respectively.

Upon averaging the data for each geometry and for each size of specimen, the plot in Figure 8 is obtained. As expected, the ligament strength decreases as the size of the structure increases. What is more interesting also is that the trend depends on the geometry of the structure. Even though the beams are made of the same mix, those with deep notches exhibit a range of variation in Figure 8, which is slightly larger than those with a small notch. Unnotched beams exhibit also a strength that is consistently higher than that of notched beams.

[††]International Union of Laboratories and Experts in Construction Materials, Systems, and Structures.
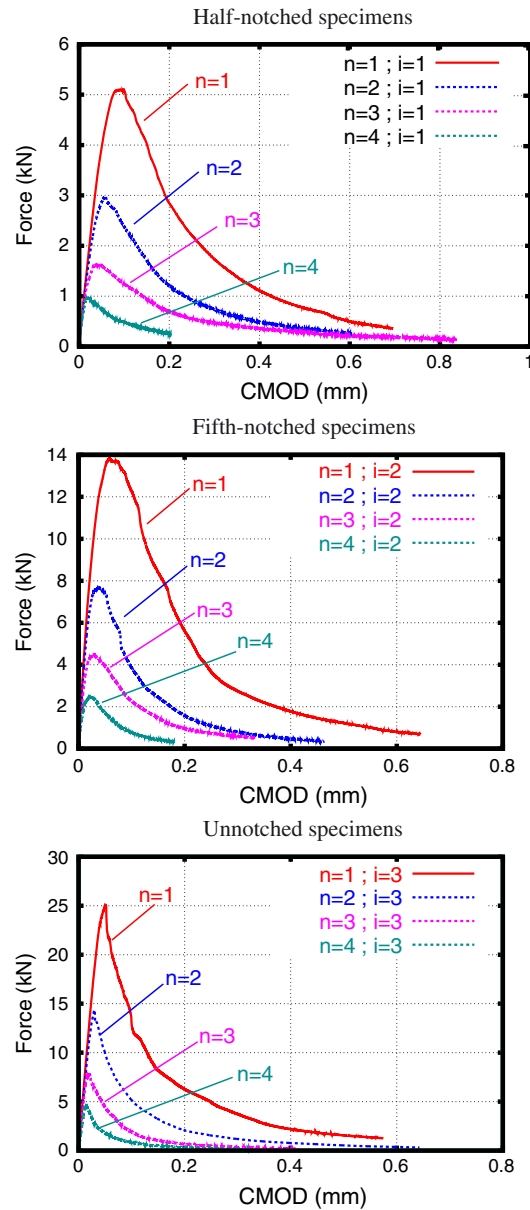
Figure 7. Averaged load versus crack mouth opening displacement (CMOD) responses (half-notched, fifth-notched and unnotched specimens).

3. NUMERICAL SIMULATIONS

Let us illustrate now how the aforementioned experimental results may be useful for assessing constitutive models for failure of concrete. As we will see, shortcomings of the constitutive model that is implemented will be emphasised.

3.1. Constitutive model

The formulation used in this paper is the integral-type non-local damage model proposed by [16]. It has been used on many occasions for the numerical simulation of size effect [27, 30, 37]. The stress–strain relation reads

$$\sigma = (1 - D)\mathrm{C} : \varepsilon \tag{2}$$

Figure 8. Comparison of the ligament strength for each size and each geometry ($D_0 = 400$ mm).

where $(\sigma, \varepsilon, \mathrm{C})$ are the stress, strain and stiffness tensors, respectively, and D is the scalar damage variable, which represents the material degradation ($D \in [0, 1]$, $D = 0$ for a virgin material and $D = 1$ for a completely damage material).
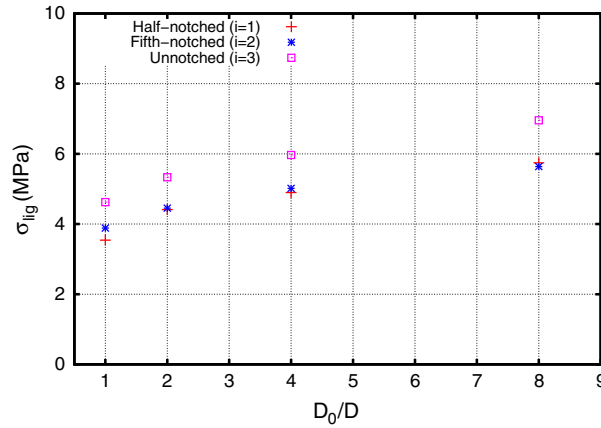
Damage is a function of the amount of extension in the material, defined locally by the equivalent strain (Equation (3)) [38].

$$\varepsilon_{\mathrm{eq}} = \sqrt{\sum_{i \in [\![1,3]\!]} \langle \varepsilon_k \rangle_+^2} \tag{3}$$

where ε_k are the principal strains ($k = 1, 2, 3$) and $\langle \varepsilon_k \rangle_+$ their positive part. The non-local equivalent strain is

$$\bar{\varepsilon}_{\mathrm{eq}} = \frac{1}{\Omega_r(x)} \int_\Omega \psi_0(x, \xi) \varepsilon_{\mathrm{eq}}(\xi) \mathrm{d}\xi \quad, \quad \Omega_r(x) = \int_\Omega \psi_0(x, \xi) \mathrm{d}\xi$$
$$\psi_0(x, \xi) = \exp\left(-\left(\frac{2||x-\xi||}{l_{c_0}}\right)^2\right) \tag{4}$$

where Ω is the volume of the structure, Ω_r is a characteristic volume introduced in such a way that the non-local operator does not affect the uniform field far away from the boundary, $\bar{\varepsilon}_{\mathrm{eq}}$ is the non-local strain, ψ_0 is a Gaussian weight function and l_{c_0} is the internal length of the non-local continuum, which is related to the size of the FPZ. Same as in Ref. [16], the part of the non-local averaging domain that protrudes outside the boundary is chopped off. Improved models can be found in the literature, with a different averaging process close to the boundary of the solid (e.g Refs [27] or [39]).

The evolution of damage (Equation (5b)) is a function of the non-local equivalent strain (Equation (4)), and it is governed by the Kuhn–Tucker loading–unloading condition (Equation (5a)).

$$\Gamma(\varepsilon, h) = \bar{\varepsilon}_{\mathrm{eq}}(\varepsilon) - h \quad, \quad \Gamma(\varepsilon, h) \leq 0 \quad, \quad \dot{h} \geq 0 \quad, \quad \dot{h}\Gamma(\varepsilon, h) = 0$$
$$h = \max(\varepsilon_{D_0}, \max(\bar{\varepsilon}_{\mathrm{eq}})) \tag{5a}$$

$$D(\bar{\varepsilon}_{\mathrm{eq}}, x) = \sum_{i \in \{t,c\}} \alpha_i \left[1 - (1 - A_i) \frac{\varepsilon_{D_0}}{\bar{\varepsilon}_{\mathrm{eq}}(x)} - A_i \exp(-B_i(\bar{\varepsilon}_{\mathrm{eq}}(x) - \varepsilon_{D_0})) \right]$$
$$\alpha_i = \sum_{k \in [\![1,3]\!]} \left(\frac{\varepsilon_k^i \langle \varepsilon_k \rangle_+}{\bar{\varepsilon}_{\mathrm{eq}}^2} \right) \tag{5b}$$

In Equation (5a), Γ is the loading function which defines the limit of the elastic (reversible) domain, ε_{D_0} is the damage threshold, h is the history variable, the largest ever reached value of the non-local equivalent strain; in Equation (5b), which defines the kinetics of damage growth, the damage variable is split into two parts to capture the differences of mechanical responses in tension ($i = t$) and in compression ($i = c$) as proposed in [38]. (α_t, α_c) are coefficients defined as functions of the principal values of the strain tensors ($\varepsilon^t, \varepsilon^c$) due to positive and negative stresses, that is, the strain tensors obtained according to Equation (2) in which the positive (resp. negative) principal stresses are retained only. Note that in uniaxial tension, $\alpha_t = 1$ and $\alpha_c = 0$, and in uniaxial compression, $\alpha_t = 0$ and $\alpha_c = 1$. (A_t, B_t, A_c, B_c) are model parameters.

3.2. Finite element model and calibration of material properties

Two-dimensional geometrically similar meshes have been designed for each configuration presented in Figure 4. The finite element meshes consist of four-node elements with four integration points. Figure 9 shows a typical mesh (514 elements) corresponding to the smallest half-notched configuration ($n = 4$, $i = 1$). To avoid mesh bias, the element size is kept constant for all specimens in the vicinity of the notch and the future FPZ, with a typical element size of (1×1.25) mm^2. Half of the specimen is meshed, taking advantage of the symmetry of the problem. The three supports are defined with fixed vertical displacement over a finite line (5 mm) to avoid spurious stress concentration effects (in the experiments, a wooden plate is placed between the support and the specimen). The computations are CMOD controlled (same as in the experiments), and the notch width is 2 mm and corresponds to one element size in each half-specimen mesh.

The Young's modulus and the Poisson's ratio used for the computations are the mean values provided in Table II: $E = 37$ GPa and $\nu = 0.21$. Damage in compression (in the upper part of the bending beams) is not expected; therefore, typical values of the model parameters in compression have been used, making sure that in uniaxial compression, the average compressive strength observed in the experiments is recovered. The threshold of damage, which is the same in tension and in compression, has been obtained from the calibration of the material parameters in tension. We obtain (A_c, B_c) = (1.15, 370).

To calibrate the model parameters in tension, the procedure outlined in Ref. [30] has been followed, considering the first three smallest sizes of specimen. An initial fit of the bending test on a notched specimen ($n = i = 2$) is achieved following a trial-and-error process. At this step, the internal length is kept constant, equal to three times the maximum aggregate size [40]. Then, the internal length has been varied until a reasonably good fit would be obtained for the three considered sizes. Note that the sensitivity analysis proposed in [30] is a guide in this iterative process. One obtains ($\varepsilon_{D_0}, A_t, B_t, l_{c_0}$) = ($10^{-5}, 0.75, 7000, 40$ mm). With this set of parameters, the response of
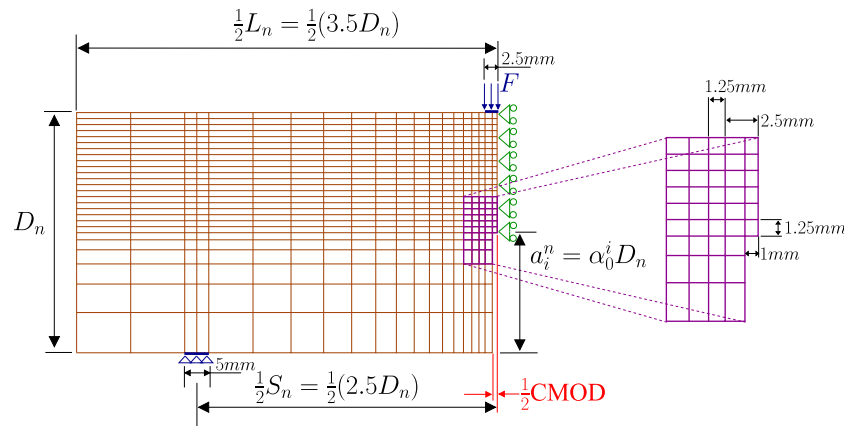

Figure 9. Mesh and boundary conditions ($n = 4$, $i = 1$). CMOD, crack mouth opening displacement.
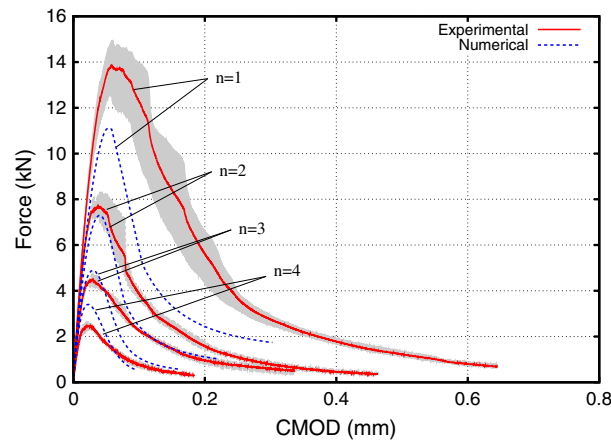
Figure 10. Capabilities of the identified model to reproduce size effect (experimental data are reproduced from Figure 7). The grey zone is the envelope of the experimental data. CMOD, crack mouth opening displacement.

the largest (fourth) beam is computed. Figure 10 shows the result of the fit on the size effect tests from the fifth-notched specimens, and the comparison for the largest specimen.

As observed on the figure, the fit might not be considered as optimum. It provides a good description of the response of the middle-size specimens, but the description of the smallest or largest specimens looses accuracy. Let us note that the final optimisation process discussed in Refs [30, 41], based for example on a Marquardt–Levenberg algorithm, has not been carried out. This calibration may, however, be considered as a sufficient approximation for the purpose of the present discussion, that is, the extension to larger sizes and different geometries.

3.3. Capabilities of the identified model to reproduce size effect on other geometries

Figure 10 shows already that the model prediction for the largest size of the same geometry is quite different from the experimental curve (peak load and softening curve). Figure 11 shows the comparison between the computations and the experiments for half-notched specimens. It is clear that the nonlocal model does not provide a good description of size effect for this geometry. Note that the reverse analysis, that is, the calibration of model parameters from data on half-notched specimens and then the
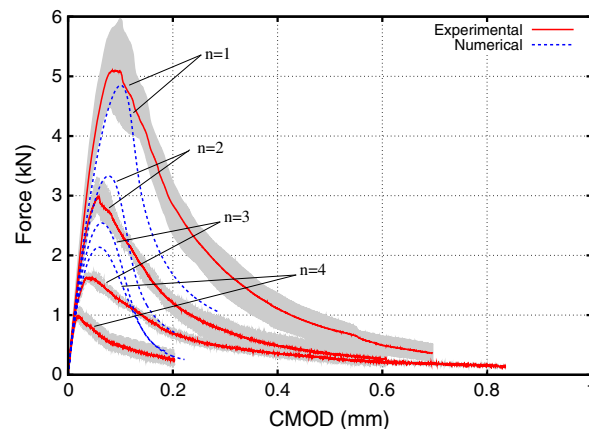

Figure 11. Description of size effect on half-notched specimens with the model parameters calibrated on size effect tests on fifth-notched specimens. The grey zone is the envelope of the experimental data. CMOD, crack mouth opening displacement.
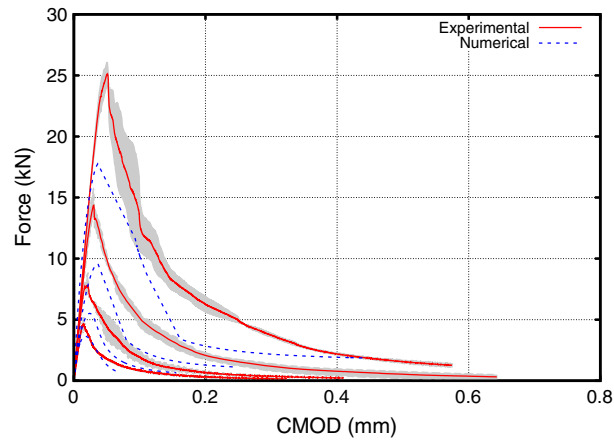
Figure 12. Description of size effect on unnotched specimens with the model parameters calibrated on size effect tests on fifth-notched specimens. The grey zone is the envelope of the experimental data. CMOD, crack mouth opening displacement.

simulation of tests on fifth-notched specimens, has been performed and yields the same deficiency. A similar deviation is also observed for the simulations on unnotched specimens (Figure 12).

4. SIZE EFFECT ANALYSIS

Prior to a detailed comparison between numerical and experimental force versus CMOD curves, a first step might be to restrict the analysis to peak loads and to comparisons with size effect formulae. This is performed in the study by [27], where it was shown that the non-local damage model was not capable of capturing size effect on the peak loads for notched and unnotched beams with the same set of model parameters. This comparison implies that size effect formulae are capable of capturing the variation of the peak loads for various sizes and various geometries in accordance with experimental data, which is what we will check in this section.

Size effect analysis of the peak loads is performed in the following according to the universal size effect law (USEL) proposed in [42]. Let us emphasise that this law has been chosen for illustrative purposes. An asset of the size effect law used herein is that it covers size effect on the structural strength of various geometries and sizes of specimens. Similar post-processing might be performed according to different size effect laws.

Following Ref. [42], the USEL (energetic format) is given in Equation (6a).

$$\sigma_N(D,\alpha_0) = \left[\frac{E'G_{\mathrm{f}}}{g_0'(\alpha_0)c_{\mathrm{f}} + g_0(\alpha_0)D}\right]^{1/2}\left[1 - \frac{rc_{\mathrm{f}}^2 g_0'' e^{-k\alpha_0^2}}{4(l_{\mathrm{p}} + D)(g_0(\alpha_0)D + g_0'(\alpha_0)c_{\mathrm{f}})}\right]^{1/r} \tag{6a}$$

with

$$\sigma_N = \frac{3}{2}\frac{PS}{bD^2} = \frac{15}{4}\frac{P}{bD} \tag{6b}$$

and

$$g(\alpha_0) = \pi\alpha_0 c_N^2 (F(\alpha_0))^2 \quad ; \quad \alpha_0 = \frac{a_0}{D} \quad ; \quad c_N = \frac{3}{2}\frac{S}{D} \quad ; \quad E' = \frac{E}{1-\nu^2} \tag{6c}$$

where σ_N is the maximum elastic stress in an unnotched beam; P is the mid-span load; S, b and D are the span, the width and the depth of the beam, respectively; E and ν are the Young's Modulus and the Poisson's ratio of the material; G_f and c_f are the fracture energy and the effective fracture process zone length (Ref. [14] for details); g and F are geometric shape functions depending on the notch-to-depth ratio α_0; c_N is the span-to-depth ratio; r and k are parameters; and l_p is a characteristic material length (Ref. [42] for details). Note that the geometry effects are included in function $g(\alpha_0)$ which is obtained from the solution of a set of elastic problems for each given geometry.

Different geometric shape functions F have been proposed in the literature. For a span-to-depth ratio of $\frac{S}{D} = 2.5$, we have for instance

$$F(x) = \sqrt{\frac{1}{\pi}} \left(\frac{1.83 - 1.65x + 4.76x^2 - 5.3x^3 + 2.51x^4}{(1+2x)(1-x)^{1.5}} \right) \text{ (from [32])} \tag{7a}$$

Table IV. Determination of the specimen size effect parameters.

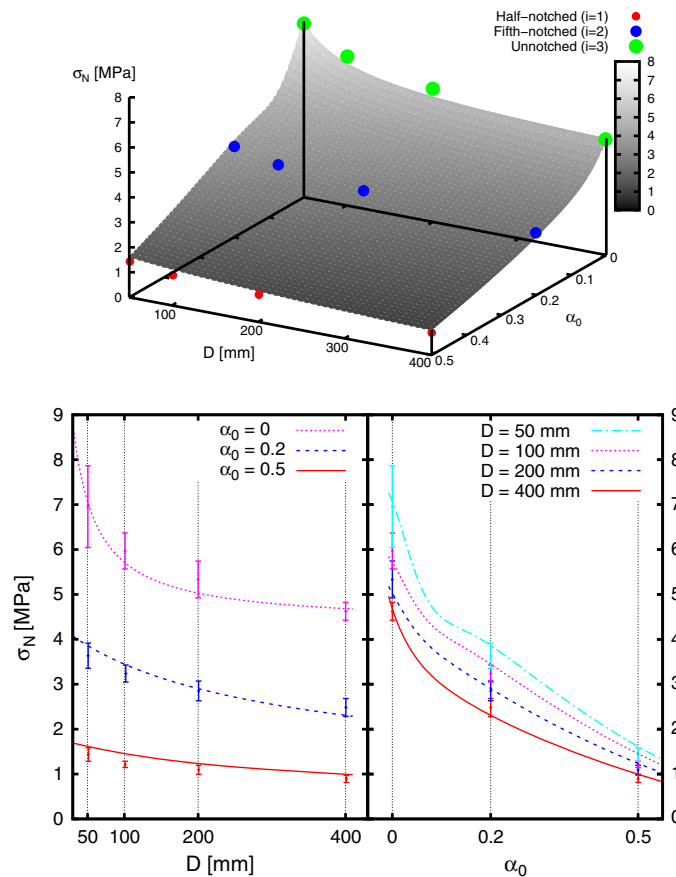| G_f	c_f	r	k	l_p	f_t
(N/m)	mm	(–)	(–)	(mm)	(MPa)
42.6	25.7	0.11	113	12.9	4.34

Figure 13. Comparison between experimental results and the Bažant's universal size effect law (see note §§ page 1446).

or

$$F(x) = \sqrt{\frac{1}{\pi} \left(\frac{p_\infty(x) + \frac{4D}{S}[p_4(x) - p_\infty(x)]}{(1 + 2x)(1 - x)^{1.5}} \right)}$$

$$\text{with} \quad p_\infty(x) = 1.989 - x(1 - x)(0.448 - 0.458(1 - x) + 1.226(1 - x)^2)$$

$$\text{and} \quad p_4(x) = 1.9 - x(-0.089 + 0.603(1 - x) - 0.441(1 - x)^2 + 1.223(1 - x)^3)$$

(8a)

(from Ref. [14] following Ref. [43])

In the following, the latter expression is chosen (Equation (8a)) because it has the advantage to be general for any span-to-depth ratio and accurate within 0.5% for any notch-to-depth ratio.

In Appendix C, Table C.1 summarises the average nominal stresses (estimated through Equation (6b)) and the average experimental peak load values.[‡‡] A non-linear Marquardt–Levenberg fit has been performed to obtain the parameters in the size effect formula. Results are presented in Table IV. From this set of parameters, the tensile strength can be estimated through Equation (9). It is consistent with the experimental splitting tensile strength in Table II. Moreover, it is indicated in Ref. [42] that the characteristic material length l_p should be approximately equal to the maximum aggregate size, which is again consistent with the grading in Figure 1. Last but not the least, the fracture energy entering in the size effect formula is consistent with the fracture energy computed according to RILEM recommendation from the load – CMOD curves in Figure 6c ($G_\mathrm{f} \approx 45$ N/m).

$$f_\mathrm{t} = c_N \sqrt{\frac{E' G_\mathrm{f}}{c_\mathrm{f} g'(0)}}$$

(9)

Figure 13[§§] presents the comparison between the experimental results presented in part 2 and the USEL given in Equation (6a) with the set of fit parameters collected in Table IV. Figure 13 shows that the USEL provides a good fit of the experimental results obtained on the three different geometries at the same time. Comparisons with experimental results corresponding to different geometries but the same materials did not exist to the authors' knowledge.

5. CONCLUSIONS

Three-point bending fracture tests investigating size effect and boundary effect for geometrically similar half-notched, fifth-notched and unnotched concrete specimens made of the same mix have been presented. The response of geometrically similar specimens is not geometrically similar, and the nominal stress depends on the structure size. Smaller structures are stronger. Moreover, the responses of notched and unnotched specimens are quite different. Such data, involving different initial notch lengths, are precious to test the capabilities of constitutive models for quasi-brittle fracture on different geometries and to validate the relevance of size effect theories as well.

The experimental results have been compared with numerical simulations performed using an integral-type non-local model. Comparisons illustrate the shortcomings of this classical formulation. The model fails to describe size effect over the investigated range of geometries and sizes. This analysis ought to be extended to other existing (and probably more advanced) constitutive models. It confirms however that there is a definite need for further investigations and enhancements of constitutive models to achieve a better description of geometry and size effect on structural failure.

Experimental results have been compared with the USEL proposed by Bažant and Yu [42] and this formula matches the experimental nominal strengths consistently.

A challenging issue is to be able to fit the entire load–displacement responses obtained and, for instance, to fit models on one geometry and to compare simulations with experimental data on other geometries. Here, it is the entire load displacement curves that should be compared, not just the peak loads. The present experimental data was elaborated more specifically for this purpose. Recent comparisons with results obtained from mesoscale models gave good prospect [44, 45].

[‡‡]The peak load values have been corrected by taking into account the weight of the specimen following [36].
[§§]Note that a 3D animated version of this figure is presented as supplementary material for a better visibility.

APPENDIX A: MECHANICAL PROPERTIES

Table A.1. Compressive tests – compressive strength.

Test #	Batch #	Height (mm)	Diameter (mm)	Ages (days)	Compressive strength (MPa)	Uncertainty (MPa)	Uncertainty (%)
171	1	308.0	160.4	102	45.2	0.4	0.9
174	1	310.0	160.3	102	45.3	0.4	0.9
252	2	218.0	119.4	125	43.5	0.2	0.3
262	2	87.9	38.8	136	48.6	0.2	0.3
351	3	219.0	115.4	185	42.5	0.2	0.3
352	3	214.0	117.4	185	37.8	0.1	0.3
453	4	215.0	116.6	185	41.4	0.2	0.3
461	4	88.1	38.8	171	39.6	0.2	0.3
561	5	96.3	38.6	168	43.3	0.2	0.3
581	5	141.9	73.6	150	42.8	0.2	0.3
682	6	140.9	73.7	169	42.8	0.2	0.3
683	6	141.9	73.6	177	42.9	0.2	0.3
751	7	213.6	113.0	145	42.4	0.2	0.3
783	7	137.7	73.6	147	38.1	0.2	0.3
852	8	213.1	112.9	145	41.5	0.2	0.3
881	8	147.5	74.3	147	39.2	0.2	0.3

Table A.2. Compressive tests – Poisson ratio.

Test #	Batch #	Height (mm)	Diameter (mm)	Ages (days)	Poisson ratio (–)	Uncertainty (–)	Uncertainty (%)
172	1	307.0	160.5	125	0.22	0.003	1
263	2	96.0	38.5	136	0.18	0.002	1
351	3	219.0	115.4	185	0.23	0.003	1
361	3	92.4	38.6	171	0.21	0.003	1
552	5	209.0	113.2	171	0.20	0.003	1
562	5	96.6	38.4	171	0.22	0.003	1
563	5	96.0	38.9	171	0.21	0.003	1
583	5	144.5	74.1	150	0.19	0.002	1
652	6	209.0	113.2	147	0.22	0.003	1
661	6	97.4	38.7	150	0.19	0.002	1
682	6	140.9	73.7	169	0.23	0.003	1
783	7	137.7	73.6	147	0.20	0.003	1

Table A.3. Compressive tests – Young modulus.

Test #	Batch #	Height (mm)	Diameter (mm)	Ages (days)	Young modulus (GPa)	Uncertainty (GPa)	Uncertainty (%)
152	1	212.2	110.8	137	38.4	0.6	1.5
153	1	191.2	112.8	102	36.5	0.6	1.6
262	2	87.9	38.8	105	37.9	0.5	1.1
263	2	96.0	38.5	136	37.5	0.5	1.1
361	3	92.4	38.6	171	35.3	0.4	1.1
362	3	91.5	38.8	172	37.8	0.51	1.1
454	4	216.0	113.7	168	36.7	0.6	1.5
461	4	88.1	38.8	171	37.3	0.5	1.1
462	4	88.6	38.6	172	36.4	0.4	1.1
551	5	219.0	117.4	171	36.2	0.6	1.5

Table A.3. *Continued.*

Test #	Batch #	Height (mm)	Diameter (mm)	Ages (days)	Young modulus (GPa)	Uncertainty (GPa)	Uncertainty (%)
552	5	209.0	113.2	171	36.5	0.6	1.5
553	5	215.0	113.6	147	37.1	0.6	1.5
583	5	144.5	74.1	150	35.4	0.4	1.1
651	6	217.7	113.7	175	37.5	0.6	1.5
652	6	209.0	113.2	147	36.8	0.6	1.5
653	6	201.5	113.1	147	37.3	0.6	1.6
681	6	141.9	73.6	149	37.9	0.4	1.1
751	7	213.6	113.0	145	37.8	0.6	1.5
762	7	83.2	38.2	147	37.7	0.5	1.1
783	7	137.7	73.6	147	37.7	0.4	1.1
786	7	143.3	74.6	158	38.4	0.4	1.1
7510	7	215.0	112.9	157	35.4	0.6	1.5
852	8	213.1	112.9	145	35.9	0.6	1.5
853	8	214.8	113.3	145	36.2	0.6	1.5
861	8	86.9	38.8	147	36.8	0.4	1.1
881	8	147.5	74.3	147	37.6	0.4	1.1
8530	8	216.4	113.1	158	37.4	0.6	1.5

Table A.4. Splitting tests – tensile strength.

Test #	Batch #	Height (mm)	Diameter (mm)	Ages (days)	Tensile strength (MPa)	Uncertainty (MPa)	Uncertainty (%)
151	1	194.0	113.2	102	3.6	0.02	0.5
172	1	307.0	160.5	125	3.9	0.03	0.6
251	2	217.0	112.8	102	3.8	0.02	0.4
353	3	197.7	111.8	185	4.3	0.02	0.4
452	4	215.0	112.6	172	3.8	0.02	0.4
554	5	217.2	113.1	150	3.8	0.02	0.4
556	5	218.1	113.2	169	4.1	0.02	0.4
654	6	216.6	113.8	150	4.1	0.02	0.4
655	6	216.4	112.9	150	3.7	0.02	0.4
656	6	218.4	112.5	169	3.8	0.02	0.4
758	7	214.7	113.2	147	3.5	0.02	0.4
857	8	210.0	113.3	147	4.2	0.02	0.4

APPENDIX B: THREE-POINT BENDING TEST RAW DATA

Table B.1. Three-point bending tests – half-notched specimens.

Test #	n #	i #	Batch #	Depth (mm)	Span (mm)	Width (mm)	Notch size (mm)	Age (days)	Peak load (kN)	Corrected peak load (kN)	Uncertainty (N)	Uncertainty (%)	Loading rate (μm/s)
111	1	1	1	400.3	1000	54.0	200.3	123	4.5	4.7	11.2	0.25	1
211	1	1	2	402.0	1000	56.1	198.6	123	5.1	5.3	12.7	0.25	1
212	1	1	2	400.8	1000	59.0	200.1	123	6.0	6.2	14.9	0.25	1
121	2	1	1	201.1	500	53.1	99.6	112	2.8	2.9	7.1	0.25	0.5
122	2	1	1	201.2	500	52.1	100.6	109	2.7	2.8	6.9	0.25	0.25
721	2	1	7	200.8	500	51.5	101.1	153	3.2	3.3	8.1	0.25	0.3

Table B.1. *Continued*

Test #	n #	i #	Batch #	Depth (mm)	Span (mm)	Width (mm)	Notch size (mm)	Age (days)	Peak load (kN)	Corrected peak load (kN)	Uncertainty (N)	Uncertainty (%)	Loading rate (µm/s)
823	2	1	8	200.7	500	52.0	101.1	152	2.9	3.3	7.4	0.25	0.3
134	3	1	1	101.0	250	50.2	50.7	122	1.7	3.0	4.3	0.25	0.5
235	3	1	2	101.0	250	50.1	50.7	119	1.6	1.7	3.9	0.25	0.5
722	2	1	7	199.9	500	51.5	101.1	153	3.3	1.6	8.2	0.25	0.4
145	4	1	1	51.7	125	49.9	25.7	122	0.9	0.9	2.4	0.25	0.25
146	4	1	1	50.9	125	49.9	25.5	122	0.9	0.9	2.4	0.25	0.25
246	4	1	2	51.0	125	50.3	25.7	122	1.1	1.1	2.8	0.25	0.25

where *n* and *i* are defined in Figure 4.
The peak load values have been corrected by taking into account the weight of the specimen following [36].

Table B.2. Three-point bending tests – fifth-notched specimens.

Test #	n #	i #	Batch #	Depth (mm)	Span (mm)	Width (mm)	Notch size (mm)	Age (days)	Peak load (kN)	Corrected peak load (kN)	Uncertainty (N)	Uncertainty (%)	Loading rate (µm/s)
511	1	2	5	400.8	1000	54.1	80.1	161	14.9	15.1	37.3	0.25	0.4
522	2	2	5	200.4	500	51.5	39.9	155	7.7	7.7	19.2	0.25	0.3
523	2	2	5	200.5	500	50.6	40.3	155	8.3	8.4	20.9	0.25	0.3
531	3	2	5	101.5	250	50.5	20.2	154	4.7	4.7	11.8	0.25	0.2
541	4	2	5	50.7	125	50.4	10.0	155	2.4	2.4	5.9	0.25	0.1
612	1	2	6	400.3	1000	53.7	80.2	161	14.6	14.8	36.5	0.25	0.4
613	1	2	6	400.0	1000	53.3	80.6	161	12.6	12.8	31.5	0.25	0.4
621	2	2	6	201.1	500	51.4	40.1	155	7.3	7.4	18.3	0.25	0.3
642	4	2	6	51.0	125	50.1	10.0	155	2.7	2.7	6.6	0.25	0.1
733	3	2	7	101.8	250	51.0	20.0	152	4.3	4.3	10.7	0.25	0.2
832	3	2	8	102.1	250	50.4	19.7	153	4.5	4.6	11.4	0.25	0.2

where *n* and *i* are defined in Figure 4.
The peak load values have been corrected by taking into account the weight of the specimen following [36].

Table B.3. Three-point bending tests – unnotched specimens.

Test #	n #	i #	Batch #	Depth (mm)	Span (mm)	Width (mm)	Notch size (mm)	Age (days)	Peak load (kN)	Corrected peak load (kN)	Uncertainty (N)	Uncertainty (%)	Loading rate (µm/s)
311	1	3	3	400.3	1000	51.5	0	181	26.0	26.2	65.1	0.25	0.4
321	2	3	3	200.2	500	51.1	0	174	14.0	14.1	35.0	0.25	0.5
322	2	3	3	199.5	500	51.2	0	175	13.7	13.7	34.2	0.25	0.3
331	3	3	3	101.0	250	50.5	0	179	8.8	8.8	21.9	0.25	0.2
341	4	3	3	50.3	125	50.3	0	180	4.3	4.3	10.7	0.25	0.1
342	4	3	3	50.8	125	49.8	0	180	5.2	5.2	13.0	0.25	0.1
413	1	3	4	400.0	1000	51.5	0	181	24.4	24.6	61.1	0.25	0.4
423	2	3	4	200.3	500	50.8	0	175	15.7	15.8	39.3	0.25	0.3
432	3	3	4	100.7	250	50.2	0	179	8.0	8.0	20.0	0.25	0.2
433	3	3	4	101.0	250	50.1	0	178	7.6	7.6	19.0	0.25	0.2

where *n* and *i* are defined in Figure 4.
The peak load values have been corrected by taking into account the weight of the specimen following [36].
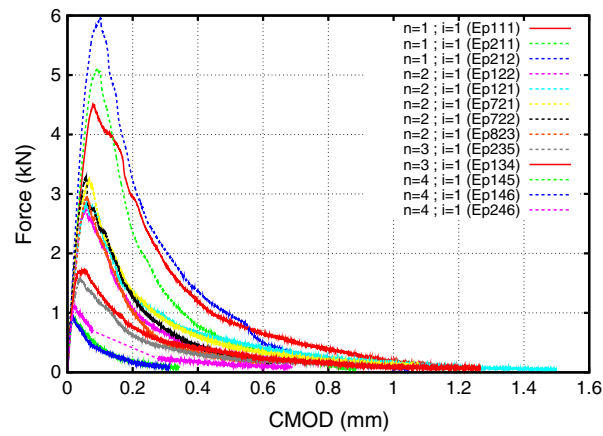
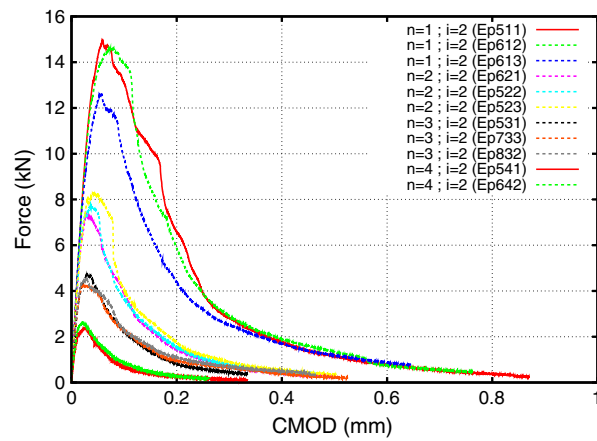Figure B.1. Force versus CMOD raw data – Half-notched specimens.

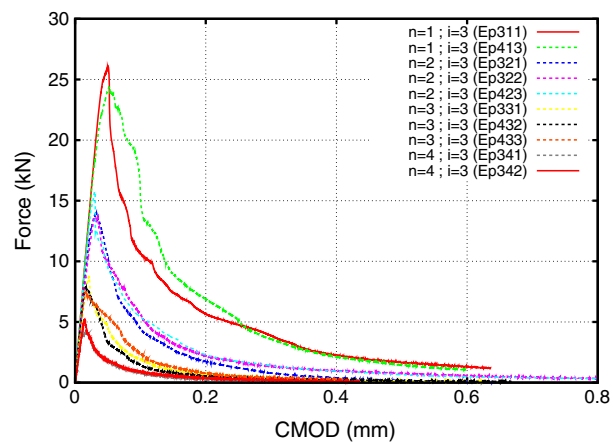Figure B.2. Force versus CMOD raw data – Half-notched specimens.

Figure B.3. Force versus CMOD raw data – unnotched specimens.

APPENDIX C: DETAILS ON SIZE EFFECT ANALYSIS

Table C.1. Nominal stress and peak load value for all specimens as defined in Equation (6b).

n #	i #	Load (F) μ (kN)	σ (kN)	c_v (%)	nominal stress (σ_N) μ (MPa)	σ (MPa)	c_v (%)	Size (D) μ (mm)	σ (mm)	c_v (%)
1	1	5.4	0.75	13.9	0.9	0.08	9.4	401.0	0.90	0.22
2	1	3.1	0.24	7.9	1.1	0.10	9.3	200.7	0.51	0.26
3	1	1.7	0.10	5.8	1.2	0.07	5.7	101.0	0.04	0.04
4	1	1.0	0.10	9.8	1.4	0.15	10.2	51.2	0.44	0.86
1	2	14.3	1.25	8.8	2.5	0.20	8.0	400.3	0.38	0.10
2	2	7.8	0.53	6.7	2.9	0.22	7.9	200.7	0.37	0.18
3	2	4.5	0.23	5.0	3.2	0.19	5.8	101.8	0.30	0.29
4	2	2.5	0.20	7.9	3.6	0.28	7.6	50.8	0.18	0.36
1	3	25.4	1.13	4.5	4.6	0.20	4.4	400.1	0.18	0.04
2	3	14.5	1.10	7.6	5.3	0.41	7.7	200.0	0.41	0.20
3	3	8.1	0.59	7.2	6.0	0.40	6.7	100.9	0.17	0.17
4	3	4.7	0.66	13.9	7.0	0.91	13.1	50.6	0.38	0.76

μ, mean value; σ, standard deviation; $c_v = \mu/\sigma$, coefficient of variation.

REFERENCES

1. Weibull W. A statistical theory of strength of materials. *Proceedings of the Royal Swedish Institute for Engineering Research* 1939; **151**:5–45.
2. Volkov S. *Statistical Strength Theory*. Gordon and Breach: New York, 1962.
3. Leicester R. Effect of size on the strength of structures. *CSIRO Australia Division of Building Research Technological Paper* 1973; **71**:1–13.
4. Walsh P. Fracture of plain concrete. *Indian Concrete Journal* 1972; **46**(11):469–470, 476.
5. Gettu R, Saldívar H, Kazemi M. Implications of the size effect method for analyzing the fracture of concrete. *International Journal of Solids and Structures* 1998; **35**(31-32):4121–4132.
6. Karihaloo B, Abdalla H, Xiao Q. Size effect in concrete beams. *Engineering Fracture Mechanics* 2003; **70**(7-8):979–993.
7. Le Bellego C, Gérard B, Pijaudier-Cabot G. Chemo-mechanical effects in mortar beams subjected to water hydrolysis. *Journal of Engineering Mechanics* 2000; **126**(3):266–272.
8. Wang Q, Zhang S, Xie H. Rock dynamic fracture toughness tested with holed-cracked flattened brazilian discs diametrically impacted by SHPB and its size effect. *Experimental mechanics* 2010; **50**(7):877–885.
9. van Vliet M, van Mier J. Experimental investigation of size effect in concrete and sandstone under uniaxial tension. *Engineering Fracture Mechanics* 2000; **65**(2-3):165–188.
10. Fischer H, Rentzsch W, Marx R. A modified size effect model for brittle nonmetallic materials. *Engineering Fracture Mechanics* 2002; **69**(7):781–791.
11. Morel S, Dourado N. Size effect in quasibrittle failure: analytical model and numerical simulations using cohesive zone model. *International Journal of Solids and Structures* 2011; **48**(10):1403–1412.
12. Luna P, Bernal C, Cisilino A, Frontini P, Cotterell B, Mai Y. The application of the essential work of fracture methodology to the plane strain fracture of ABS 3-point bend specimens. *Polymer* 2003; **44**(4):1145–1150.
13. Bažant Z. Size effect in blunt fracture: concrete, rock, metal. *Journal of Engineering Mechanics* 1984; **110**(4): 518–535.
14. Bažant Z, Planas J. *Fracture and Size Effect in Concrete and Other Quasibrittle Materials*. CRC: Boca Raton, Florida, 1998.
15. Carpinteri A. Fractal nature of material microstructure and size effects on apparent mechanical properties. *Mechanics of Materials* 1994; **18**(2):89–101.
16. Pijaudier-Cabot G, Bažant Z. Nonlocal damage theory. *Journal of Engineering Mechanics* 1987; **113**(10): 1512–1533.

17. Peerlings R, De Borst R, Brekelmans W, De Vree J. Gradient enhanced damage for quasi-brittle materials. *International Journal for Numerical Methods in Engineering* 1996; **39**(19):3391–3403.
18. Wells G, Sluys L. A new method for modelling cohesive cracks using finite elements. *International Journal for Numerical Methods in Engineering* 2001; **50**(12):2667–2682.
19. Moës N, Belytschko T. Extended finite element method for cohesive crack growth. *Engineering Fracture Mechanics* 2002; **69**(7):813–833.
20. Oliver X, Huespe A, Samaniego E, Chaves E. Continuum approach to the numerical simulation of material failure in concrete. *International Journal for Numerical and Analytical Methods in Geomechanics* 2004; **28**:609–632.
21. Tvergaard V, Needleman A. Effects of nonlocal damage in porous plastic solids. *International Journal of Solids and Structures* 1995; **32**(8-9):1063–1077.
22. Bažant Z, Jirásek M. Nonlocal integral formulations of plasticity and damage: survey of progress. *Journal of Engineering Mechanics* 2002; **128**:1119.
23. Grassl P, Jirásek M. Plastic model with non-local damage applied to concrete. *International Journal for Numerical and Analytical Methods in Geomechanics* 2006; **30**(1):71–90.
24. Saanouni K, Chaboche J, Lesne P. On the creep crack-growth prediction by a non local damage formulation. *European Journal of Mechanics. A. Solids* 1989; **8**(6):437–459.
25. Germain N, Besson J, Feyel F. Composite layered materials: anisotropic nonlocal damage models. *Computer Methods in Applied Mechanics and Engineering* 2007; **196**(41-44):4272–4282.
26. Simone A, Askes H, Sluys L. Incorrect initiation and propagation of failure in non-local and gradient-enhanced media. *International Journal of Solids and Structures* 2004; **41**(2):351–363.
27. Krayani A, Pijaudier-Cabot G, Dufour F. Boundary effect on weight function in nonlocal damage model. *Engineering Fracture Mechanics* 2009; **76**(14):2217–2231.
28. Grégoire D, Rojas-Solano L, Pijaudier-Cabot G. Continuum to discontinuum transition during failure in non-local damage models. *International Journal of Multiscale Computational Engineering* 2012; **10**(6):567–580.
29. Jirasek M, Rolshoven S, Grassl P. Size effect on fracture energy induced by non-locality. *International Journal for Numerical and Analytical Methods in Geomechanics* 2004; **28**(7-8):653–670.
30. Le Bellégo C, François Dubé J, Pijaudier-Cabot G, Gérard B. Calibration of nonlocal damage model from size effect tests. *European Journal of Mechanics-A/Solids* 2003; **22**(1):33–46.
31. Carmeliet J. Optimal estimation of gradient damage parameters from localization phenomena in quasi-brittle materials. *Mechanics of Cohesive-frictional Materials* 1999; **4**(1):1–16.
32. Tang T, Bažant Z, Yang S, Zollinger D. Variable-notch one-size test method for fracture energy and process zone length. *Engineering Fracture Mechanics* 1996; **55**(3):383–404.
33. Duan K, Hu X, Wittmann F. Scaling of quasi-brittle fracture: boundary and size effect. *Mechanics of Materials* 2006; **38**(1-2):128–141.
34. Bažant Z, Li Z. Zero-brittleness size-effect method for one-size fracture test of concrete. *Journal of Engineering Mechanics* 1996; **122**(5):458–468.
35. Biolzi L, Labuz J, Muciaccia G. A problem of scaling in fracture of damaged rock. *International Journal of Rock Mechanics and Mining Sciences* 2010; **48**(3):451–457.
36. Bažant Z. Size-effect method for determining fracture energy and process zone size of concrete. *Materials and Structures* (submitted by RILEM Committee TC 89-FMT, chaired by S.P. Shah) 1990; **23**(6):461–465.
37. Mazars J, Pijaudier-Cabot G, Saouridis C. Size effect and continuous damage in cementitious materials. *International Journal of Fracture* 1991; **51**(2):159–173.
38. Mazars J. A description of micro- and macroscale damage of concrete structures. *Engineering Fracture Mechanics* 1986; **25**(5-6):729–737.
39. Bažant Z, Le J, Hoover C. Nonlocal boundary layer (nbl) model: overcoming boundary condition problems in strength statistics and fracture analysis of quasibrittle materials. In *Fracture Mechanics of Concrete and Concrete Structures Recent Advances in Fracture Mechanics of Concrete (Proc., FraMCoS-7, 7th Int. Conf. held in Jeju, Korea, plenary lecture)*, Oh B-H (ed.). Korea Concrete Institute: Seoul, 2010; 135–143.
40. Bažant Z, Pijaudier-Cabot G. Measurement of characteristic length of nonlocal continuum. *Journal of Engineering Mechanics* 1989; **115**(4):755–767.
41. Iacono C, Sluys L, van Mier J. Estimation of model parameters in nonlocal damage theories by inverse analysis techniques. *Computer Methods in Applied Mechanics and Engineering* 2006; **195**(52):7211–7222.
42. Bažant Z, Yu Q. Universal size effect law and effect of crack depth on quasi-brittle structure strength. *Journal of Engineering Mechanics* 2009; **135**:78.
43. Pastor J, Guinea G, Planas J, Elices M. Nueva expresión del factor de intensidad de tensiones para la probeta de flexión en tres puntos. *Anales de Mecánica de la Fractura* 1995; **12**:85–90.
44. Grassl P, Grégoire D, Rojas-Solano L, Pijaudier-Cabot G. Meso-scale modelling of the size effect on the fracture process zone of concrete. *International Journal of Solids and Structures* 2012; **49**:1818–1827.
45. Grégoire D, Grassl P, Rojas-Solano L, Pijaudier-Cabot G. Macro and mesoscale models to predict concrete failure and size effects. In *Damage Mechanics of Cementitious Materials and Structures*, Pijaudier-Cabot G, Dufour F (eds). ISTE Ltd: London and John Wiley & Sons, Inc.: Hoboken, 2012.